

REPORT DOCUMENTATION PAGE

Form Approved OMB NO. 0704-0188

The public reporting burden for this collection of information is estimated to average 1 hour per response, including the time for reviewing instructions, searching existing data sources, gathering and maintaining the data needed, and completing and reviewing the collection of information. Send comments regarding this burden estimate or any other aspect of this collection of information, including suggestions for reducing this burden, to Washington Headquarters Services, Directorate for Information Operations and Reports, 1215 Jefferson Davis Highway, Suite 1204, Arlington VA 22202-4302. Respondents should be aware that notwithstanding any other provision of law, no person shall be subject to any penalty for failing to comply with a collection of information if it does not display a currently valid OMB control number.
PLEASE DO NOT RETURN YOUR FORM TO THE ABOVE ADDRESS.

1. REPORT DATE (DD-MM-YYYY)	2. REPORT TYPE Technical Report	3. DATES COVERED (From - To) -		
4. TITLE AND SUBTITLE Annual Report 2013-2014		5a. CONTRACT NUMBER W911NF-12-1-0501		
		5b. GRANT NUMBER		
		5c. PROGRAM ELEMENT NUMBER 611102		
6. AUTHORS Changyong Qin, Jerry Whitten		5d. PROJECT NUMBER		
		5e. TASK NUMBER		
		5f. WORK UNIT NUMBER		
7. PERFORMING ORGANIZATION NAMES AND ADDRESSES Benedict College Office of Research 1600 Harden St. Columbia, SC 29204 -1058		8. PERFORMING ORGANIZATION REPORT NUMBER		
9. SPONSORING/MONITORING AGENCY NAME(S) AND ADDRESS (ES) U.S. Army Research Office P.O. Box 12211 Research Triangle Park, NC 27709-2211		10. SPONSOR/MONITOR'S ACRONYM(S) ARO		
		11. SPONSOR/MONITOR'S REPORT NUMBER(S) 62613-EL-H.8		
12. DISTRIBUTION AVAILABILITY STATEMENT Approved for public release; distribution is unlimited.				
13. SUPPLEMENTARY NOTES The views, opinions and/or findings contained in this report are those of the author(s) and should not be construed as an official Department of the Army position, policy or decision, unless so designated by other documentation.				
14. ABSTRACT 2013-2014 Annual Report				
15. SUBJECT TERMS Anual Report				
16. SECURITY CLASSIFICATION OF: a. REPORT UU		17. LIMITATION OF ABSTRACT b. ABSTRACT UU	15. NUMBER OF PAGES	19a. NAME OF RESPONSIBLE PERSON Changyong Qin
				19b. TELEPHONE NUMBER 803-705-4582

Report Title

Annual Report 2013-2014

ABSTRACT

2013-2014 Annual Report

Annual Report July 8, 2014

Theoretical Studies of Nerve Agents Adsorbed on Surfaces

Jerry L Whitten

Professor of Chemistry
North Carolina State University
Raleigh, NC 27695

Telephone Number: 919-515-7960

Email: whitten@ncsu.edu

Collaborating Institution: Benedict College, Co-PI, Dr. CY Qin

Abstract

This report examines fundamental processes involving the interaction of nerve agents with solid surfaces using accurate electronic structure methods. The objective is to describe surface interactions and low energy electronic states accurately and to identify factors that affect desorption energies and kinetics, solvation of nerve agents by water and the spectral features of adsorbed nerve agents. Understanding exactly how these molecules interact with organic films and oxide surfaces is the primary goal of this work. Initial work on sarin adsorbed on aliphatic and aromatic hydrocarbon surfaces and on a calcium oxide surface has been completed. Studies of the solvation of sarin by water are underway. The results should clarify how water affects desorption properties and the extent of solvation of the nerve agent as it leaves the surface. Preliminary solvation results are included in the report. One paper, submitted for publication in J. Physical Chemistry, is undergoing minor revision to address question raised in the review. A second paper on the solvation studies is being written.

1. Overview of Research

In this work, we examine fundamental processes involving the interaction of nerve agents with solid surfaces using accurate electronic structure methods. Adsorption on several types of surfaces found in structural materials are considered for two types of nerve agents: sarin, a nerve gas, (see Fig. 1) and VX type nerve agents . Although both nerve agents are organophosphates, they differ in the ester linkage and in substituent groups. These differences are known to lead to different persistence times on surfaces.

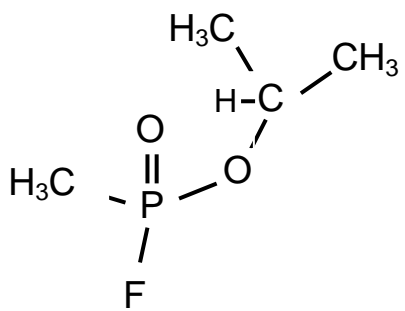


Fig. 1. Sarin nerve gas. An organophosphate nerve agent with an ester linkage to an aliphatic group.

The objective of the work is to describe surface interactions and low energy electronic states at high accuracy using theory in order to understand the details of bonding to surfaces. The plan is to carry out the study so that factors that affect desorption energies, desorption kinetics and the spectral features of adsorbed nerve agents can be quantified. Understanding exactly how these molecules interact with a variety of solid surfaces is the primary goal of this work.

The project is divided into three phases:

1) Adsorption of sarin on hydrocarbon and oxide surfaces

2) Solvation of sarin adsorbed on surfaces by water

3) Study of the nerve agent VX and examination of the low lying excited states of sarin adsorbed on surfaces.

Phase 1 has been completed and Phase 2 is nearing completion. The project benefitted from the participation of two sabbatical leave visitors to the Whitten group from Athens, Greece, G. Petsalakis and I. Petsalakis. The visitors had prior experience using Density Functional Theory to describe molecule-surface interactions and this permitted a comparison of DFT and our many-electron CI calculations for sarin bound to hydrocarbon and oxide surfaces.

Appendix I contains the manuscript describing the results from Phase 1 of the project. This manuscript was submitted to J. Phys. Chem. and is currently undergoing minor revision to clarify questions raised in the review.

In the Phase 2 solvation studies, the surfaces are either initially coated by water, see for example the snapshot in Fig. 2, followed by introduction of sarin at a series of distances from the surface, or the sarin molecule is solvated first, see Fig. 3, and then allowed to approach the surface. In both cases, sarin and the surface compete for the water molecules and the molecules move optimally to solvate both sarin and the surface as the molecule approaches the surface. We follow the energetics of the system as a function of the distance of sarin from the surface allowing the water molecules to move to their minimum energy location for each choice of sarin position. The results should lead to an understanding of the effect of water solvation on the ability of a surface to retain sarin.

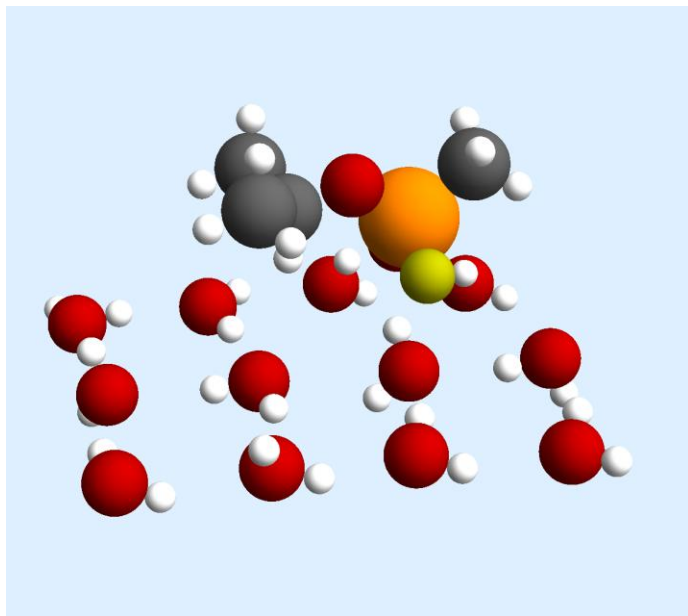


Fig. 2. Binding directly to water layer: 16 kcal/mol

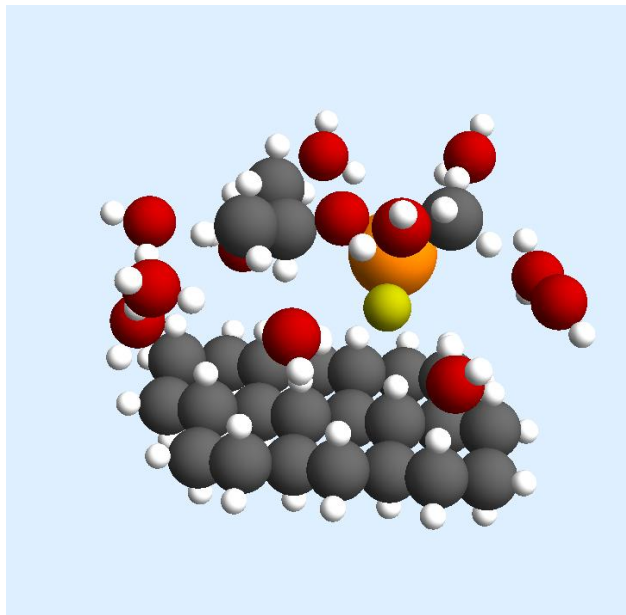


Fig. 3. Solvation of sarin near an aliphatic hydrocarbon surface by water.

Appendix

J. Phys. Chem. paper

CI and DFT Studies of the Adsorption of the Nerve Agent Sarin on Surfaces

Brian N. Papas,^a Ioannis D. Petsalakis,^{a,b} Giannoula Theodorakopoulos^{a,b} and Jerry L. Whitten^a

^aDepartment of Chemistry, North Carolina State University, Raleigh, North Carolina, 27695, USA.

^bTheoretical and Physical Chemistry Institute, The National Hellenic Research Foundation, 48 Vass. Constantinou Ave. Athens 116 35 Greece.

ABSTRACT: A theoretical study is presented on the adsorption of the sarin molecule, a nerve agent, on three model solid surfaces: aliphatic (graphane), aromatic (graphene), and ionic (CaO). Calculations are carried out using accurate electronic structure methods based on Configuration Interaction (CI) as well as complementary Density Functional Theory (DFT) and Time Dependent DFT calculations. The objective is to describe surface interactions accurately in order to identify factors that affect adsorption of sarin. Potential energy curves are calculated and compared between surface types. Computed CI binding energies to graphane, graphene, and calcium oxide surfaces are 2.4, 5.2, and 13.2 kcal/mol, respectively. The corresponding DFT binding energies are 6.4, 4.8, and 18.8 kcal/mol, respectively. Excited states of free sarin as well as sarin bound to the surfaces are examined using TDDFT and CI. Low-lying excited states of the adsorption complexes involving excitations from the surface to sarin are calculated.

1. INTRODUCTION

In this work, we examine fundamental processes involving the interaction of sarin (isopropyl methylphosphonofluoridate), a nerve agent molecule depicted in Fig. 1, with aliphatic, aromatic, and polar surfaces using accurate electronic-structure methods of configuration interaction (CI) and density functional theory (DFT). Sarin is a member of a class of organophosphate (OP) nerve agents that differ in ester linkage and substituent groups. The objective of this work is to describe surface interactions at high accuracy using theory in order to understand the details of bonding of sarin to common surfaces. Detailed insight into the surface chemistry of chemical warfare agents (CWAs) is critical to the rational design of advanced filters and decontamination strategies for these extremely toxic compounds.

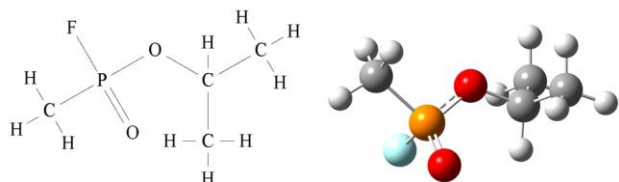


Figure 1. Sarin nerve gas. An organo-phosphate nerve agent with an ester linkage to an aliphatic group. Coloring scheme as follows: C (gray), H (white), O (red), P (orange), F (blue).

Most nerve agents act by disrupting the enzymatic degradation of the neurotransmitter acetylcholine. The organophosphates are known to bind nearly irreversibly to acetylcholinesterase, thereby blocking the channel for acetylcholine decomposition and recycling. The resulting buildup of acetylcholine over-stimulates nerve action leading to fatal contractions of muscles.

The same molecular characteristics that cause tight binding to acetylcholinesterase may be involved in bonding to structural materials. It is useful to consider first the interactions qualitatively. Strong interactions involving the phosphate region and ester linkages can induce ionic or polar interactions with a solid surface, and presumably this would leave the molecule free to later desorb as an intact molecule. Strong covalent bonding, however, may disrupt the molecular structure and leave the agent inactive. Substituent groups can give rise to a stabilizing van der Waals bonding with any surface, and if only this type of bonding were involved, one would expect that the adsorbed molecule could be easily removed from the surface. Understanding quantitatively, at the molecular level, the interactions of sarin with the different surfaces and the excited states of the adsorption complexes are the main objectives of the present investigation.

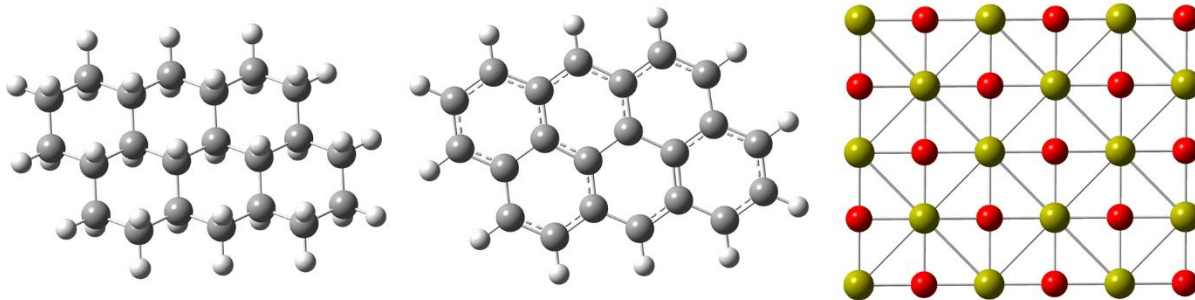


Figure 2. Model surfaces employed in the CI calculations. Left-to-right: graphane, graphene, calcium oxide. Covalent radii used for atom size. Coloring scheme as follows: C (gray), H (white), O (red), Ca (yellow).

Two types of hydrocarbon surfaces and calcium oxide are adopted as models:

1. Graphane – a surface with CH dipoles and low polarizability.
2. Graphene – polycyclic aromatics show intermediate reactivity and the potential for large dipole and charge induced polarizations.
3. Calcium oxide – the ionic solid limit where strong interactions with the phosphate and ester regions of the nerve agents are anticipated. Calcium oxide surfaces have similar ionic charge distributions to calcium carbonates. Carbonates and silicates are major components of structural materials.

A great deal of experimental and computational work has been devoted to adsorption and interaction of OP warfare agents or stimulants with different surfaces, including silica,^{1, 2} carbonaceous nanoporous materials, and metal-oxide surfaces.³⁻⁸ To the author's knowledge, adsorption of sarin on the surfaces of the present work, graphane, graphene and CaO, has not been previously considered, while there exists a previous theoretical investigation of sarin physisorbed as well as chemisorbed on model MgO surfaces.⁶ The structure of gas phase sarin has also been investigated extensively⁹⁻¹⁷ by spectroscopic methods and by electronic-structure calculations. Furthermore, dissociation of sarin in the lowest triplet and singlet excited states has been investigated¹⁶ in response to a report of destructive elimination of sarin with the aid of UV irradiation.^{14, 15}

2. THEORETICAL METHODS

Two types of electronic structure approaches are employed: the first one involves configuration interaction along with a simplex optimization method for the geometry optimizations. The second approach involves density functional theory (DFT) calculations for the ground electronic state and time dependent DFT (TDDFT) calculations for excited electronic states, with details given below.

2.1. Many-electron CI Theory

The adsorbate-surface systems will be described by a configuration interaction embedding method that is designed to give an accurate many-electron description of the adsorbate-surface region for both ground and excited electronic states. Many applications to adsorbates on metals and oxides have been reported previously and details can be found in Ref. 18-21. In the case of small particles, there is no need to make approximations in the coupling of the local region to the bulk and in this case “embedding” refers to the creation of an electronic subspace that is treated by configuration interaction. A brief summary of the theory is given below.

Calculations are carried out for the full electrostatic Hamiltonian of the system

$$H = \sum_i^N \left[-\frac{1}{2} \nabla_i^2 + \sum_k^Q \left(\frac{-Z_k}{r_{ik}} \right) \right] + \sum_{i < j}^N \frac{1}{r_{ij}}$$

Wavefunctions are constructed by self-consistent-field (SCF) and multi-reference configuration interaction (CI) expansions,

$$\Psi = \sum_k c_k (n!)^{1/2} \det (\chi_1^k \chi_2^k \dots \chi_n^k) = \sum_k c_k \Phi_k$$

Single and double excitations from an initial representation of the state of interest, Φ_r , are carried out to create a small CI expansion,

$$\Psi'_r = \Phi_r + \sum_{ijkl} \lambda_{ijkl} \Gamma_{ij \rightarrow kl} \Phi_r = \sum_m \Phi_m$$

Configurations, Φ_k , are retained if the interaction with Φ_r satisfies a relatively large threshold condition

$$|\langle \Phi_k | H | \Phi_r \rangle|^2 / |E_k - E_r| > 10^{-4} \text{ a.u.}$$

Next, we refine the description of the state by generating a large CI expansion, Ψ_r , by single and double excitations from all important members of Ψ'_r (those with coefficient > 0.05) to obtain

$$\Psi_r = \Psi'_r + \sum_m [\sum_{ik} \lambda_{ikm} \Gamma_{i \rightarrow k} \Phi_m + \sum_{ijkl} \lambda_{ijklm} \Gamma_{ij \rightarrow kl} \Phi_m]$$

where Φ_m is an important member of Ψ'_r . The additional configurations are generated by identifying and retaining all configurations, Φ_k , that interact with Ψ'_r such that

$$|\langle \Phi_k | H | \Psi'_r \rangle|^2 / |E_k - E_r| > 3 \times 10^{-7} \text{ a.u.}$$

For this small threshold, typically 4×10^4 configurations occur in the final CI expansion, and the expansion can contain single through quadruple excitations from an initial representation of the state Φ_r . Contributions of configurations not explicitly retained are estimated using perturbation theory.

In order to accelerate the convergence of the CI expansion results with respect to active space size for the excited state calculations, the molecular orbitals of the lowest triplet state for each system are first put through a unitary transformation. This transformation creates a set of occupied and virtual orbitals which have maximal exchange interaction with the occupied orbitals within the active space. The primary function of this is to allow accurate description of the states of interest in the presence of less accurately described lower-lying states. The basis of this argument lies in the way other configurations are generated from the states of interest. For a given excited state, Ψ_r , allowing all single and double excitations from its important configurations also generates all lower lying states that have significant interaction with Ψ_r . Since these configurations are in principle included in the diagonalization, it follows that the excited state, Ψ_r , is orthogonal to and non-interacting with lower energy states. Thus the variational theorem for excited states is satisfied.

For the CI computations, the interaction of sarin is described using fixed-geometry surfaces sufficiently large enough to ensure that sarin would remain fully over the surface and not interact appreciably with boundary atoms. These surface models, depicted in a subsequent figure, correspond to $C_{22}H_{12}$ for graphene, $C_{22}H_{34}$ for graphane, and $Ca_{15}O_{15}$ for calcium oxide.

Compact, but still flexible bases were used in this study, and can roughly be characterized as double-zeta plus polarization.²² These are described as $(10s5p1d) \rightarrow [4s2p1d]$ for C and O, $(12s8p1d) \rightarrow [6s4p1d]$ for P, $(10s5p) \rightarrow [4s2p]$ for F, and $(5s1p) \rightarrow [2s1p]$ for H. For the graphane surface only the p_z orbital was added to each H atom to ensure sufficient bond polarization. Graphene hydrogen atoms did not use any p functions, while the carbon atoms had additional diffuse s and p_z functions added with exponents of 0.08. For calcium oxide the surface should

show little reaction to the addition of sarin and so a (22s12p)→[5s2p] basis for Ca and a (12s5p)→[2s1p] basis for O were used. This basis was generated by minimizing the total energy of Ca₄O₄, and is given in the supplemental information.

2.2. Simplex Optimization Method

The CI geometry optimizations are carried out by the Nelder-Mead simplex procedure.²³ The optimization allows variation of the geometry of adsorbates on the surfaces of interest. In the simplex procedure, the parameters that define the geometry are taken as components of a so-called vertex or n-tuple. The energy is calculated for that vertex and a systematic variation of the parameters is carried out in a way that eliminates the worst vertex after each iteration. The procedure is widely used in applied mathematics and is surprisingly robust. It has an advantage in that energy gradients are not required and the energy minimization can be carried out directly at the CI level of theory since only a computer code capable of computing the energy is needed. The latter point is important when electron correlation has a significant effect on the geometry, e.g., stretched bonds or pre-dissociation. Geometry optimizations at the CI level allowed all degrees of freedom of sarin to vary, while keeping the model surfaces locked at a standard geometry.

2.3. DFT and TDDFT Calculations

Complementary to the CI calculations described in Section 2.1 DFT²⁴ and TDDFT²⁵ calculations employing the M062X functional^{26, 27} and two types of basis sets, 6-31G(d,p) and 6-311G+(d,p) (i.e. including diffuse functions) have been carried out on sarin adsorbed on graphene, graphane and CaO, as in the CI calculations but using slightly different models for the surfaces. The smaller basis set was employed for larger models of the surfaces, cf., structures (a) and (d) for graphene (C₆₆H₂₂) and graphane (C₆₆H₈₈), respectively, and structure (g) for CaO in Figure 3. The larger basis set was employed for smaller models of the graphene (C₂₈H₁₄) and graphane (C₂₈H₄₂) surfaces, (b) and (e), respectively, in Figure 3, and also for the CaO (Ca₁₅O₁₅) surface, (h). Binding energies of sarin on the three surfaces have been determined, taking into account the basis superposition error. In addition, excited states and absorption spectra of the adsorption complexes of sarin on graphene and graphane have been calculated and compared to the absorption spectrum of free sarin obtained by TDDFT/M062X/6-311+G(d,p). For further comparison, the absorption spectrum of isolated sarin has been calculated by TDDFT employing nine additional functionals (specified in Figure 4) and the 6-311+G(d,p) basis set. Corresponding data has been generated by CI calculations for free sarin as well as the adsorption complexes.

Geometry optimization of the adsorption complexes involved first the optimization of the surface and subsequently optimization of the adsorbed sarin. In the case of CaO, inclusion of 5 atoms on the surface in the second step of the optimization resulted in 2.3 kcal/mol increased binding energy.

Finally, DFT/M062X calculations have also been carried out for sarin on MgO ($Mg_{15}O_{15}$) (cf. (h) in Figure 3), for comparison with previous work on this system.⁶ For these calculations basis sets 6-31G(d,p) and 6-311G(d,p) have been employed. Addition of diffuse functions was not possible as the calculations did not converge. For comparison, the previous work employed 6-31G(d) basis set with DFT/B3LYP and MP2 calculations on different models of sarin on MgO.⁶ All the DFT and TDDFT calculations of the present work have been carried using Gaussian 09.²⁸

3. RESULTS

3.1. Sarin Geometries

Four conformers of sarin were optimized at the CI level. The minimum energy structure of sarin used in the present study is depicted in Figure 1. This is the geometry labeled sarin II reported in Ref. 17. The energy of this geometry is less than 1 kcal/mol above the minimum energy geometry reported in Ref. 17, and thus for the purposes of this research is considered unimportant. The remaining conformers differed by rotation of the aliphatic and phosphate regions and changes in the central C-O-P bond angle.

3.2. Binding Geometries

3.2.1. Overview

In Figure 3 the structures of the adsorption complexes obtained by DFT and CI are given; in Table 1 the calculated binding energies are collected. These results will be discussed below starting with the comparatively simplest case of sarin on CaO.

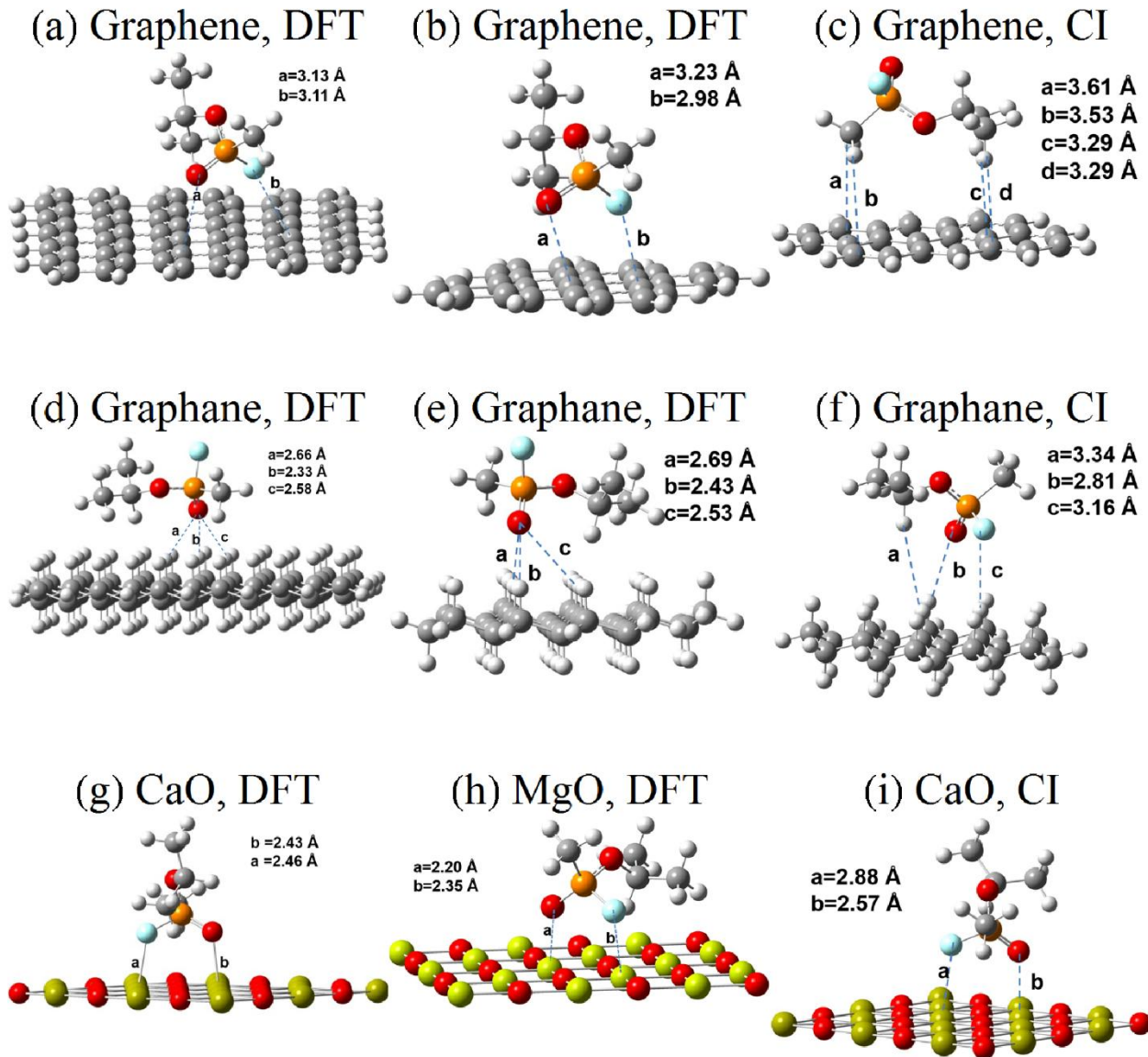


Figure 3. Optimum geometries of the adsorption complexes of sarin on graphene, (a) and (b) obtained by DFT and (c) by CI, on graphane, (d) and (e) by DFT and (f) by CI, on CaO, (g) by DFT and (i) by CI and on MgO (h) by DFT, cf. text.

3.2.2. Sarin on CaO

Figures 3g–i show optimal binding geometries of sarin to oxide surfaces. The binding appears to be a straight-forward electrostatic interaction. The P atom of sarin aligns with an O atom of the surface, and the F and terminal O atoms align over Ca atoms, creating pairs of opposite charges. The center of mass of sarin is 4.04 Å above the surface in the CI calculations.

In all calculations, the Ca-O/F distance is on the order of 2.4 Å. All calculations are in good agreement on the binding energy (Table 1), with all results in the range of 10–20 kcal/mol. Relaxation of the CaO lattice during binding was found to have negligible impact on the binding energy using DFT. For comparison, reported values of binding energy of sarin on MgO, calculated by B3LYP/6-31G(d) and a large model ($Mg_{16}O_{16}$) is 2.9 kcal/mol while that obtained by MP2/6-31G(d) and a small cluster (Mg_4O_4) is 50 kcal/mol.⁶ It should be noted that in the present work the MgO was modelled with M062X on a single layer of $Mg_{15}O_{15}$, not two layers as in the previous work. As shown in Table 1, significant binding of 20.0 kcal/mol is obtained for sarin on MgO, consistent with the expectation of stronger binding of sarin to MgO than CaO.

Table 1. Calculated binding energy (BE) of sarin at different surfaces by DFT and CI.

Surface (structure of Figure 3) /basis set	BE (kcal/mol)	BSSE-corrected BE (kcal/mol)
Graphene (a)/ 6-31G(d,p)	6.7	-
Graphene (b)/ 6-31G(d,p)	6.4	2.6
Graphene (b)/ 6-311+G(d,p)	8.2	4.8, 5.2*
Graphane (d)/ 6-31G(d,p)	9.0	-
Graphane (e)/ 6-31G(d,p)	7.9	4.9
Graphane (e)/ 6-311+G(d,p)	8.5	6.4, 2.4*
CaO (g)/ 6-31G(d,p)	33.9	16.1
CaO (g)/ 6-311+G(d,p)	22.3	18.8, 13.2*
MgO (h)/6-31G(d,p)	32.8	19.3
MgO (h)/6-311G(d,p)	31.8	20.0

*Corresponding CI value

3.2.3. Sarin on graphene

Unlike the results for CaO, DFT and CI give different binding geometries for sarin on graphene (Figure 3a–c). Specifically, DFT models predict binding through the sarin oxygen and fluorine atoms, while CI predicts a flipped orientation, cf. Figure 3b vs 3c. Consistency between the M062X/6-31G(d,p) results for large (Fig. 3a) and middle-sized (Fig 3b) graphene surfaces suggests that the M062X/6-311+G(d,p) binding energy of 4.8 kcal/mol should be taken as accurate. Despite the difference in orientation, there is good agreement with the CI computed binding energy of 5.2 kcal/mol. Cross-examinations of the two orientations with the two levels of theory indicate that the energy difference between the two orientations is small (about 0.1–0.4 kcal/mol, depending on the model), with the optimum geometry being dependent on the particulars of the method used. It should be noted that in both orientations the dipole moment of sarin is directed perpendicular to the graphene surface.

3.2.4. Sarin on graphane

Of the three surfaces modelled, graphane exhibits the greatest discrepancy between the DFT and CI results. From the DFT results, sarin binds with its oxygen atom down and 2.3 Å from a nearest surface hydrogen atom, and its fluorine atom pointed away from the surface (Fig. 3d,e). Predicted binding is on the order of 6 kcal/mol – slightly greater than that of sarin on graphene. The CI computations suggest a binding with the sarin oxygen and fluorine atoms at the surface (Fig. 3f), but a binding of only 2.4 kcal/mol. Investigation of the orientation of sarin on graphane obtained by CI employing the CI model ($C_{22}H_{34}$), as well as the larger ($C_{28}H_{42}$) model, using the DFT/M062X method show that for the smaller CI model only the CI structure (cf. (f) of Figure 3) is obtained whereas with the larger model the DFT structure, cf. (e) in Figure 3, is favored. Therefore there is a significant effect of the size of the model employed on the calculated orientation of the adsorption complex.

3.3. Excited States

A great deal of experimental and theoretical work has been devoted to the determination of the lowest energy structure of sarin and other warfare agents in the ground electronic state, but the excited states have not been studied very extensively.⁵ For sarin, a low intensity absorption is reported with the threshold electronic excitation occurring in the vacuum-UV (~7.1 eV or higher) with varying theoretical estimates, eg. 7.38 eV obtained by TDDFT/B3LYP/6-311+G(2df,p) and 9.9 eV by MP2/6-31+G(d) calculations.⁹ Here too we find a varying excitation energy for the lowest singlet excited state of free sarin, depending on the functional employed in TDDFT/6-311+G(d,p) calculations . In Figure 4 the absorption spectra of free sarin obtained by TDDFT calculations and ten different functionals, offered in Gaussian 09, are shown. The lowest onset for the electronic excitations is obtained with the PBEPBE functional at 6.6 eV and the highest with M062X at 8.1 eV. Generally low oscillator strengths are calculated with all functionals employed. CI calculations on the excited state employing the basis set previously described lead to an excitation energy of 9.1 eV, i.e., comparable to an earlier MP2/6-31+G(d) result.⁹ However, inclusion of a single diffuse s function (exponent of 0.01) in the phosphorus atom basis set allows an accurate CI estimate of the lowest Rydberg excitations. These come in at 8.0 eV and 8.5 eV, corresponding to excitations from the oxygen/fluorine lone-pair manifold into a Rydberg state. This is in good agreement with the present CAM-B3LYP and M062X TDDFT results on the spectrum of free sarin, cf. Figure 4

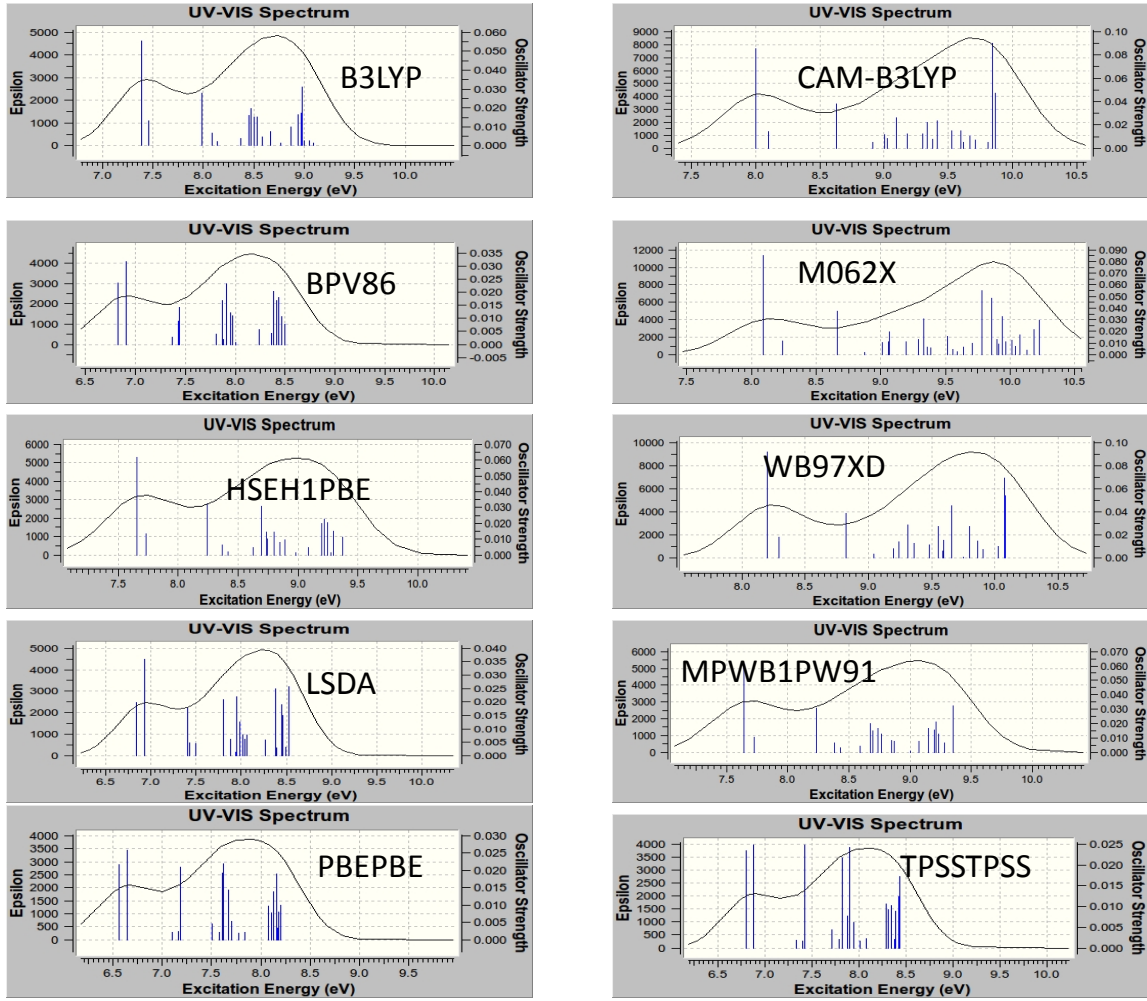


Figure 4. Adsorption spectra of free sarin calculated by TDDFT employing different functionals, as indicated.

Next, the absorption spectra of sarin adsorbed on graphene and graphane were considered using TDDFT/M062X and the 6-311+G(d,p) basis set. For the graphene-sarin system the lowest 50 roots were calculated in the region 1.98 eV – 6.19 eV, none of which correspond to the sarin-sarin excitation. The lowest transitions correspond to graphene-graphene excitations. There also exist a number of charge-transfer type excitations, from occupied orbitals of graphene to unoccupied orbitals of sarin. For example, states calculated at 3.37 and 4.2 eV involve excitations into a Rydberg unoccupied orbital of sarin. Other such states are found at 5.5, 6.08, 6.18 and 6.19 eV. The calculations on graphane-sarin involved the lowest 20 roots. In this case the lowest unoccupied orbital or LUMO is a Rydberg orbital of sarin and is involved in several excited states of the complex. In particular, the lowest excited state at 6.4 eV, which is characterized by the HOMO→LUMO excitation, corresponds to an excitation from graphane to

sarin. As was the case for graphene-sarin, the calculations did not reach any sarin-sarin excited states. It should be noted that the above calculations on the excited states of the adsorption complexes, just as in the case of free sarin, required inclusion of diffuse functions in the basis set. With the 6-31G(d,p) basis set the first 25 roots of the CaO-sarin calculation correspond to excitations involving only the surface. Calculations with the 6-311+G(d,p) basis on the CaO-sarin complex were not practical.

CI Computations in which the dominant component of the excitation was restricted to be into the Rydberg orbital of sarin were used to determine the transition energy of the lowest lying surface-to-sarin electron transfer excitation. For graphane, the lowest is at 7.0 eV; the remainder are above the free sarin excitation. The numerous low-lying virtual orbitals on graphene proved a significant challenge for isolating the charge-transfer excitation, and the best estimate places it near 5.3 eV. Excitations from the central portion of the CaO model surface (excitations from orbitals localized on the edges of the model were disallowed) provided a set of ten electron-transfer possibilities ranging in transition energy from 6.2 eV to 8.5 eV. Therefore, with both methods, the existence of charge-transfer excited states at energies lower than the sarin-sarin excitation is indicated. Similar observations have been reported for sarin and other organophosphorus warfare agents adsorbed on a $\gamma\text{-Al}_2\text{O}_3$ surface.⁵

4. CONCLUSIONS

Our results indicate that the polarized phosphate region of the sarin molecule plays a critical role in its binding to aliphatic, aromatic, and oxide surfaces. Specifically, the Lewis-base portion acts as the binding agent. For the surfaces considered in the present study, only those that are ionic (CaO) or have large polarizability (graphene) give strong binding for sarin. Binding to aliphatic surfaces is weak. Figure 5 depicts CI potential curves for interaction of sarin with the three model surfaces.

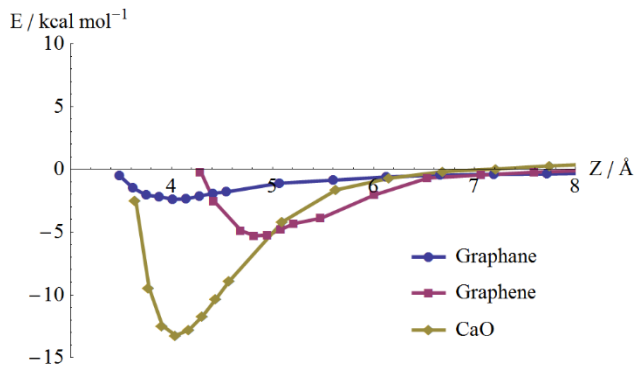


Figure 5. Potential curves for sarin interaction with three model surfaces. Infinite separation limit is free sarin in minimum energy geometry and bare surface. The z-axis corresponds to the height of the sarin center-of-mass above the highest atom of surface.

It is concluded that

- Sarin binds to graphane, graphene, and calcium oxide surfaces by 2.4, 5.2, and 13.2 kcal/mol, respectively according to CI, with corresponding DFT binding energies 6.4, 4.8, and 18.8 kcal/mol, respectively.
- Free sarin has an excitation into a Rydberg state at about 8 eV.
- Each of the three surfaces studied is capable of transferring an electron to sarin at or below the sarin Rydberg excitation. Both DFT and many-electron computational methods gave similar results, with TDDFT capable of determining a greater total number of roots, and CI capable to giving accurate results for specific states of interest.

5. ACKOWLEDGEMENTS

Support of this research by the U.S. Army Research Office is gratefully acknowledged.

6. REFERENCES

1. Wilmsmeyer, A. R.; Gordon, W. O.; Davis, E. D.; Troya, D.; Mantooth, B. A.; Lalain, T. A.; Morris, J. R., Infrared Spectra and Binding Energies of Chemical Warfare Nerve Agent Simulants on the Surface of Amorphous Silica. *Journal of Physical Chemistry C* 2013, 117, 15685-15697.
2. Troya, D.; Edwards, A. C.; Morris, J. R., Theoretical Study of the Adsorption of Organophosphorous Compounds to Models of a Silica Surface. *Journal of Physical Chemistry C* 2013, 117, 14625-14634.
3. Kowalczyk, P.; Gauden, P. A.; Terzyk, A. P.; Neimark, A. V., Screening of carbonaceous nanoporous materials for capture of nerve agents. *Physical Chemistry Chemical Physics* 2013, 15, 291-298.
4. Patil, L. A.; Bari, A. R.; Shinde, M. D.; Deo, V.; Kaushik, M. P., Detection of dimethyl methyl phosphonate - a simulant of sarin: The highly toxic chemical warfare - using platinum activated nanocrystalline ZnO thick films. *Sensors and Actuators B-Chemical* 2012, 161, 372-380.
5. Bermudez, V. M., Computational Study of Environmental Effects in the Adsorption of DMMP, Sarin, and VX on gamma-Al₂O₃: Photolysis and Surface Hydroxylation. *Journal of Physical Chemistry C* 2009, 113, 1917-1930.
6. Michalkova, A.; Ilchenko, M.; Gorb, L.; Leszczynski, J., Theoretical study of the adsorption and decomposition of sarin on magnesium oxide. *Journal of Physical Chemistry B* 2004, 108, 5294-5303.
7. Michalkova, A.; Paukku, Y.; Majumdar, D.; Leszczynski, J., Theoretical study of adsorption of tabun on calcium oxide clusters. *Chemical Physics Letters* 2007, 438, 72-77.

8. Paukku, Y.; Michalkova, A.; Leszczynski, J., Adsorption of dimethyl methylphosphonate and trimethyl phosphate on calcium oxide: an ab initio study. *Structural Chemistry* 2008, 19, 307-320.
9. Rauk, A.; Shishkov, I. F.; Vilkov, L. V.; Koehler, K. F.; Kostyanovsky, R. G., DETERMINATION OF THE STRUCTURE AND CHIROPTICAL PROPERTIES OF THE PARENT NERVE-GAS O-METHYL METHYLPHOSPHONOFUORIDATE BY AB-INITIO CALCULATIONS, ELECTRON-DIFFRACTION ANALYSIS, AND NMR-SPECTROSCOPY. *Journal of the American Chemical Society* 1995, 117, 7180-7185.
10. Koskela, H., A set of triple-resonance nuclear magnetic resonance experiments for structural characterization of organophosphorus compounds in mixture samples. *Analytica Chimica Acta* 2012, 751, 105-111.
11. Christesen, S. D.; Jones, J. P.; Lochner, J. M.; Hyre, A. M., Ultraviolet Raman Spectra and Cross-Sections of the G-series Nerve Agents. *Applied Spectroscopy* 2008, 62, 1078-1083.
12. DaBell, R. S.; Suenram, R. D.; Lavrich, R. J.; Lochner, J. M.; Ellzy, M. W.; Sumpter, K.; Jensen, J. O.; Samuels, A. C., The geometry of organophosphonates: Fourier-transform microwave spectroscopy and ab initio study of diethyl methylphosphonate, diethyl ethylphosphonate, and diisopropyl methylphosphonate. *Journal of Molecular Spectroscopy* 2004, 228, 230-242.
13. Mott, A. J.; Rez, P., Calculated infrared spectra of nerve agents and simulants. *Spectrochimica Acta Part a-Molecular and Biomolecular Spectroscopy* 2012, 91, 256-260.
14. Zuo, G.-M.; Cheng, Z.-X.; Shi, W.-P.; Zhang, X.-H.; Zhang, M., Photoassisted removal of sarin vapor in air under UV light irradiation. *Journal of Photochemistry and Photobiology a-Chemistry* 2007, 188, 143-148.
15. Zuo, G.-M.; Cheng, Z.-X.; Li, G.-W.; Shi, W.-P.; Miao, T., Study on photolytic and photocatalytic decontamination of air polluted by chemical warfare agents (CWAs). *Chemical Engineering Journal* 2007, 128, 135-140.
16. Xu, C.-X.; Zuo, G.-M.; Cheng, Z.-X.; Han, J., Computational Study Toward Understanding the Photodissociation Mechanism of Sarin. *International Journal of Quantum Chemistry* 2011, 111, 4410-4417.
17. Kaczmarek, A.; Gorb, L.; Sadlej, A. J.; Leszczynski, J., Sarin and soman: Structure and properties. *Structural Chemistry* 2004, 15, 517-525.
18. Papas, B. N.; Whitten, J. L., Dissociation of Water on a Palladium Nanoparticle. *International Journal of Quantum Chemistry* 2010, 110, 3072-3079.
19. Papas, B. N.; Whitten, J. L., Silver as an electron source for photodissociation of hydronium. *Journal of Chemical Physics* 2011, 135.
20. Papas, B. N.; Whitten, J. L., Excitonic states in a (Ti₆O₁₂)₍₃₎ nanotube. *Journal of Chemical Physics* 2013, 138, 6.

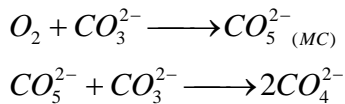
21. Whitten, J. L.; Yang, H., Theory of chemisorption and reactions on metal surfaces. *Surface Science Reports* 1996, 24, 59-124.
22. Whitten, J. L., Gaussian Lobe Function Expansions of Hartree-Fock Solutions for First-Row Atoms and Ethylene. *Journal of Chemical Physics* 1966, 44, 359-&.
23. Nelder, J. A.; Mead, R., A SIMPLEX-METHOD FOR FUNCTION MINIMIZATION. *Computer Journal* 1965, 7, 308-313.
24. Parr, R. G.; Yang, W. T., DENSITY-FUNCTIONAL THEORY OF THE ELECTRONIC-STRUCTURE OF MOLECULES. *Annual Review of Physical Chemistry* 1995, 46, 701-728.
25. Marques, M. A. L.; Gross, E. K. U., Time-dependent density functional theory. *Annual Review of Physical Chemistry* 2004, 55, 427-455.
26. Zhao, Y.; Truhlar, D. G., Density functionals with broad applicability in chemistry. *Accounts of Chemical Research* 2008, 41, 157-167.
27. Zhao, Y.; Truhlar, D. G., The M06 suite of density functionals for main group thermochemistry, thermochemical kinetics, noncovalent interactions, excited states, and transition elements: two new functionals and systematic testing of four M06-class functionals and 12 other functionals. *Theoretical Chemistry Accounts* 2008, 120, 215-241.
28. Frisch, M. J.; Trucks, G. W.; Schlegel, H. B.; Scuseria, G. E.; Robb, M. A.; Cheeseman, J. R.; Scalmani, G.; Barone, V.; Mennucci, B.; Petersson, G. A.; Nakatsuji, H.; Caricato, M.; Li, X.; Hratchian, H. P.; Izmaylov, A. F.; Bloino, J.; Zheng, G.; Sonnenberg, J. L.; Hada, M.; Ehara, M.; Toyota, K.; Fukuda, R.; Hasegawa, J.; Ishida, M.; Nakajima, T.; Honda, Y.; Kitao, O.; Nakai, H.; Vreven, T.; Montgomery, J. A., Jr.; Peralta, J. E.; Ogliaro, F.; Bearpark, M.; Heyd, J. J.; Brothers, E.; Kudin, K. N.; Staroverov, V. N.; Kobayashi, R.; Normand, J.; Raghavachari, K.; Rendell, A.; Burant, J. C.; Iyengar, S. S.; Tomasi, J.; Cossi, M.; Rega, N.; Millam, N. J.; Klene, M.; Knox, J. E.; Cross, J. B.; Bakken, V.; Adamo, C.; Jaramillo, J.; Gomperts, R.; Stratmann, R. E.; Yazyev, O.; Austin, A. J.; Cammi, R.; Pomelli, C.; Ochterski, J. W.; Martin, R. L.; Morokuma, K.; Zakrzewski, V. G.; Voth, G. A.; Salvador, P.; Dannenberg, J. J.; Dapprich, S.; Daniels, A. D.; Farkas, Ö.; Foresman, J. B.; Ortiz, J. V.; Cioslowski, J.; Fox, D. J. *Gaussian 09, Revision D.01*, Gaussian, Inc.: Wallingford CT, 2009.

Oxygen Reduction by Molten Carbonate in Solid Oxide Fuel Cells

Changyong Qin, PhD
Benedict College, Columbia, SC 29204

1. Overview of Tasks

In the current funded period, the oxygen reduction reaction (ORR) in the cathode of solid oxide fuel cells (SOFC) by molten carbonate (MC) was further explored using DFT methods. Previous studies indicate that the formation of peroxocarbonate (CO_4^{2-}) is a key process in ORR and the formed reaction intermediate serves as a carrier of oxygen in MC. Simply, CO_4^{2-} can be treated as an atomic oxygen attached to one carbonate. The migration of oxygen in MC has been studied by DFT, showing the oxygen in the form of CO_4^{2-} has lower reduction potential than oxygen molecule and can migrate in MC with low barrier of energy.



In this part, we calculated the formation of CO_4^{2-} as a two step process (Equations above). First, molecular oxygen captured by a carbonate and forms CO_5^{2-} , then another carbonate will be reacted with CO_5^{2-} to form two CO_4^{2-} . Transition states were located on the potential energy surface (PES) and intrinsic reaction coordinate (IRC) calculations show the reaction process as indicated by the equations above.

The DFT calculated results will be applied to the studies by the configuration interaction (CI) method. In particular, the optimized structures will be used for CI calculations. The CI wavefunction will then be used to analyze the chemical process and compared to the DFT results. The direct comparison will validate the accuracy of DFT and assure the use of right hybrid functional(s) when DFT is applied to such systems. More importantly, the CI method using charge localization method will allow to examine the bonding and energy of charged molecules in MC or on cathode surfaces.

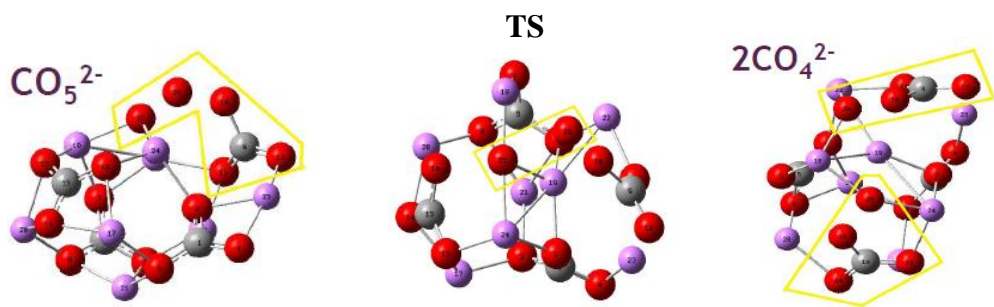
2. Results and Discussions

2.1 Formation of CO_4^{2-} in MC

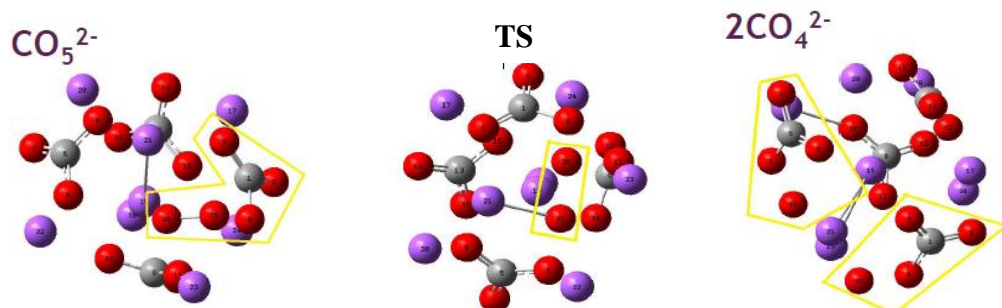
The binding of oxygen to carbonate forms CO_5^{2-} , the optimized structure of CO_5^{2-} (Figure 1) is very close to that in gas phase reported and only negligible change was detected. This CO_5^{2-} will then react with another carbonate to form CO_4^{2-} as shown in the equations below.

For step two, a transition state (Figure 1) was located on the potential energy surface (PES) for each type of MC. At TS, the O-O distance is increased to about 2.0 Å, indicative of a breaking O-O bond. IRC calculations (Figure 2) show the energy barriers and confirm the reaction path. More details will be included in the manuscript under preparation. The shift of one oxygen to the other carbonate causes the dissociation of oxygen attached to one carbonate, which makes two independent CO_4^{2-} , which then serves as oxygen carrier.

(A) $\text{O}_2\text{-}(\text{Li}_2\text{CO}_3)_4$



(B) $\text{O}_2\text{-}(\text{Na}_2\text{CO}_3)_4$



(A) $\text{O}_2\text{-}(\text{K}_2\text{CO}_3)_4$

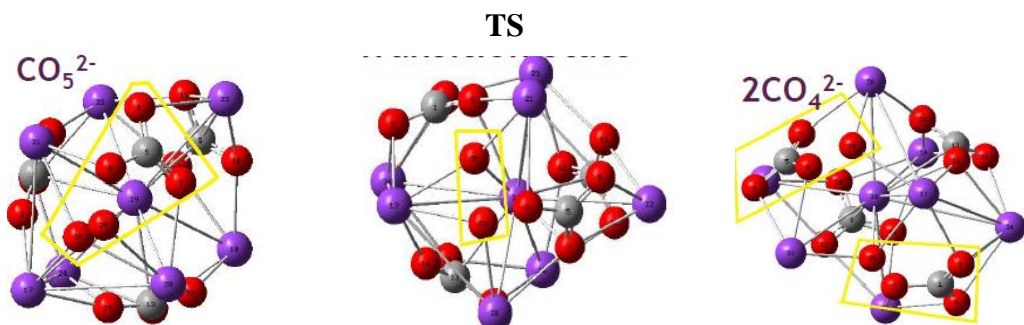


Figure 1: Optimized structures of CO_5^{2-} , TS, and 2CO_4^{2-} in MC

(O-O distance: $\sim 1.4\text{\AA}$ in CO_5^{2-} , $\sim 2.0\text{\AA}$ in TS, and $>3.0\text{\AA}$ in 2CO_4^{2-})

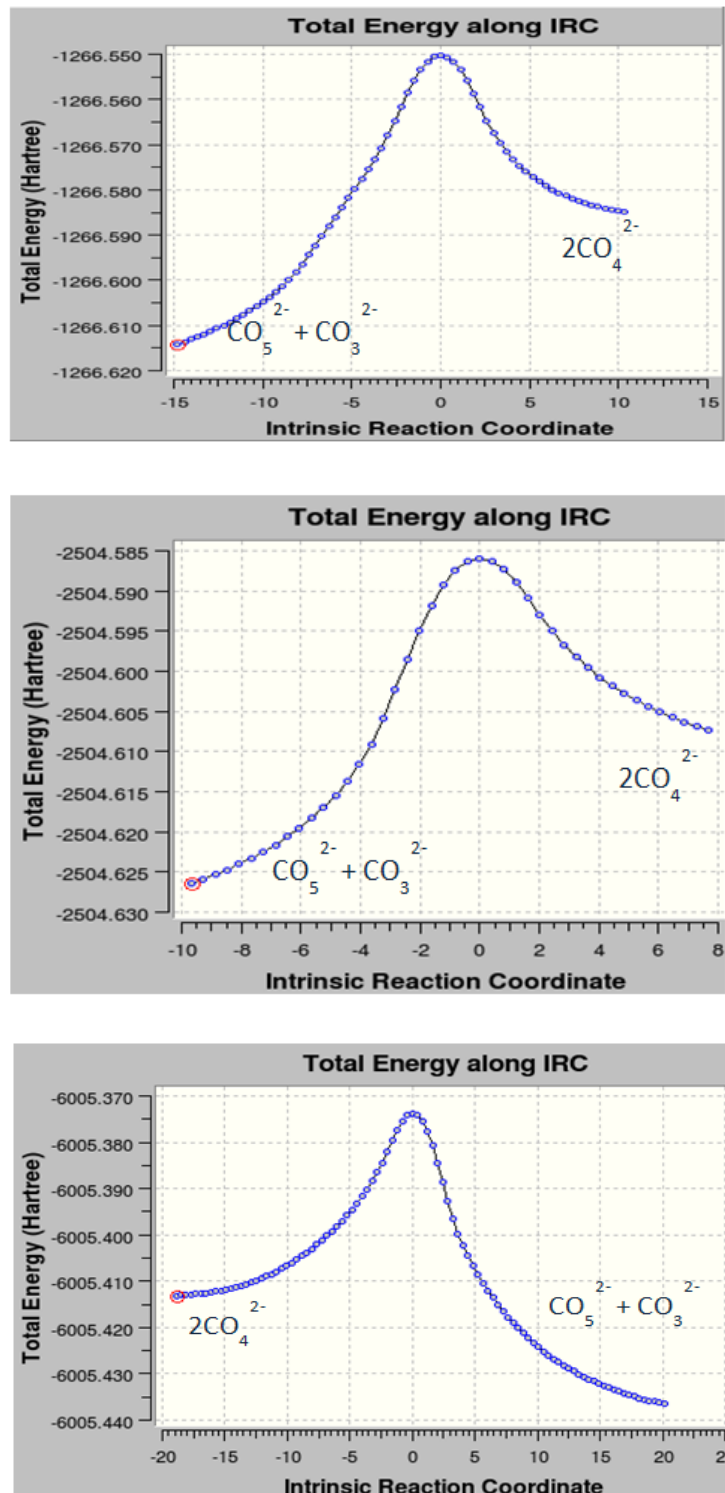


Figure 2: PES of $\text{CO}_5^{2-} + \text{CO}_3^{2-} \leftrightarrow 2\text{CO}_4^{2-}$ (Top: Li₂CO₃, Middle: Na₂CO₃, Bottom: K₂CO₃)

The energy barrier of oxygen dissociation to form CO_4^{2-} is estimated to be 49, 28, 41 kcal/mol in Li, Na, K MC, respectively. This finding needs confirmation from experiments and also further modeling with different methods will be performed to confirm if sodium carbonate will benefit the ORR process more than lithium and potassium carbonate salts.

2.2 New Oxygen Reduction Mechanism by DFT Modeling

Combining the experimental and computational results, the evidences point to that oxygen reduction is through the formation of CO_4^{2-} in MC. This active oxygen form will accept electrons and release an oxide and carbonate. Previous studies show the oxygen can easily shift between two neighboring carbonates, which means the oxygen diffusion in MC is very effective. The full reaction path is displayed in Figure 3.

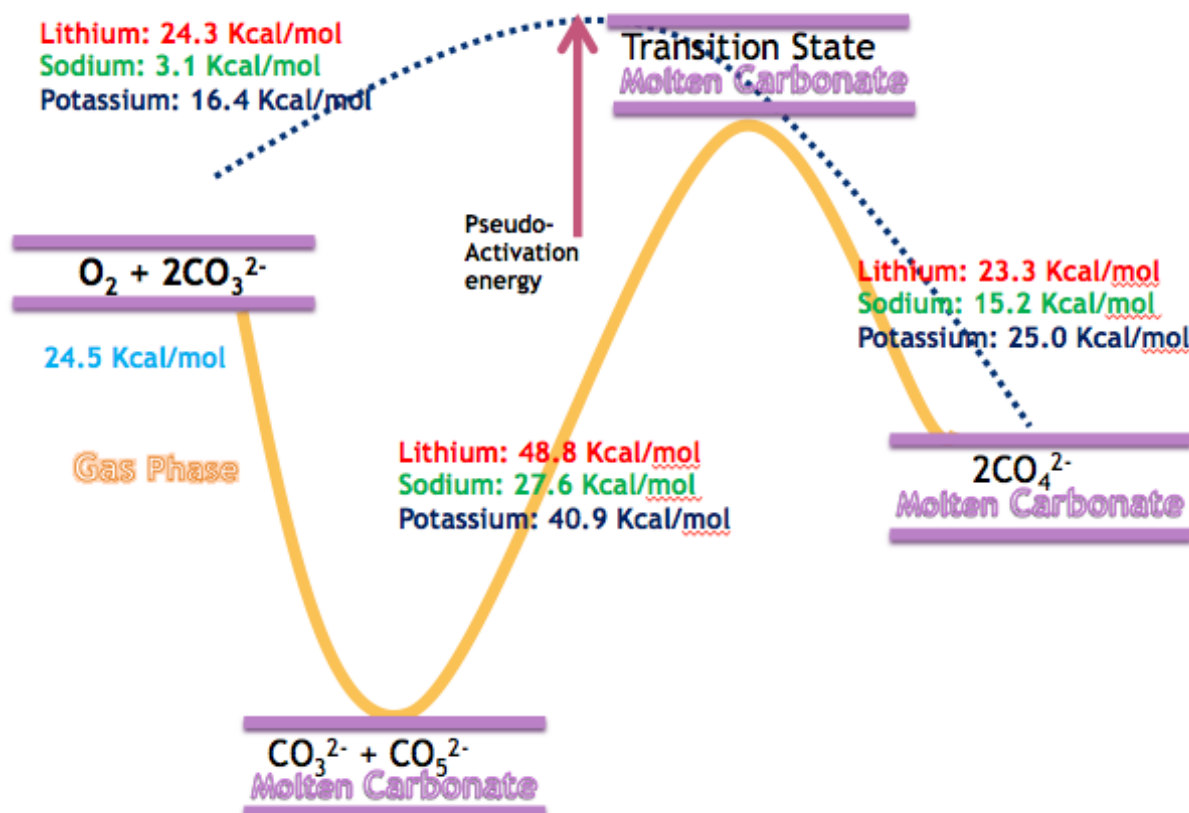


Figure 3: Formation of CO_4^{2-} by Oxygen in MC

(The energy barrier for overall reaction is calculated to be

24.3 kcal/mol, 3.1 kcal/mol and 16.4 kcal/mol)

2.3 Raman and DFT study of pyrocarbonate

2.3.1 In-situ Raman spectroscopic investigation

The Li_2CO_3 and Na_2CO_3 eutectic mixture (52:48 in mol%) was first synthesized in air at 650°C . After a 2-h hold, the melt was then quenched to room temperature, followed by breaking it into fine particles by ball milling. Thus prepared powders were then packed into a gold crucible that was subsequently loaded into a high temperature stage (Linkam TS1500, $0^\circ\text{C}\sim1500^\circ\text{C}$). The temperature and gas were controlled by a system controller (Linkam PE95). The Raman spectra were recorded with a LabRam/HR confocal Raman system (LabRam Invers, Horiba Jobin-Yvon) with a He-Ne laser operated at 632.8 nm. Since the position of the thermal couples in the high temperature stage is located outside the crucible, the actual and the controlled temperatures of the MC are different. The melting point of the of $(\text{Li}/\text{Na})_2\text{CO}_3$ at 490°C was used to calibrate the actual temperature. The scattering Raman spectra were collected *in-situ* from the carbonate as a function of temperature (in the range of RT- 600°C) and atmosphere (in N_2 , air, CO_2).

2.3.2 DFT modeling

DFT calculations were performed at the B3LYP/6-31G(d) level using Gaussian09 suite of quantum programs. The geometry of $\text{Li}_2\text{C}_2\text{O}_5$ and $\text{Na}_2\text{C}_2\text{O}_5$ were optimized first, and the vibrational frequencies were then obtained from analytic second derivatives using a harmonic oscillator model. In addition, Raman intensities were computed by numerical differentiation of dipole derivatives with respect to the electric field.

2.3.3 Temperature dependence of Raman spectrum

Figure 4 (a) shows the Raman spectra collected from a eutectic $\text{Li}_2\text{CO}_3\text{-Na}_2\text{CO}_3$ (52 mol% $\text{Li}_2\text{CO}_3\text{-Na}_2\text{CO}_3$) melt over a band range of $650\text{-}1,850\text{ cm}^{-1}$ as a function of temperatures in a pure CO_2 atmosphere. For the carbonate in solid state, the Raman spectra are seen to contain four basic vibrational modes relevant to CO_3^{2-} ions. The two bands at $1,078$ and $1,094\text{ cm}^{-1}$ are assigned to v_1 of symmetric stretching vibrations in Li_2CO_3 and Na_2CO_3 , whereas the bands at 792 cm^{-1} and 870 cm^{-1} are assigned to v_2 of out-of-plane bending vibrations. For the isolated CO_3^{2-} that has a D_{3h} symmetry, v_2 is Raman inactive. However, it is likely that v_2 becomes Raman active for $(\text{Li}/\text{Na})_2\text{CO}_3$ due to the distortion of the CO_3^{2-} structure imposed by the cations. The observed bands at 704 and 728 cm^{-1} are assigned to v_4 of in-plane bending vibrations. This mode is a double degeneration for the distorted CO_3^{2-} induced by Li^+ and Na^+ . As the CO_3^{2-} group becomes distorted from its regular planer symmetry, this mode splits into two components. The bands at $1,375\text{ cm}^{-1}$, $1,404\text{ cm}^{-1}$, $1,531\text{ cm}^{-1}$ and $1,563\text{ cm}^{-1}$ are attributed to a split v_3 of the asymmetric stretching vibrations caused by the existence of Li^+ and Na^+ around the CO_3^{2-} ions.

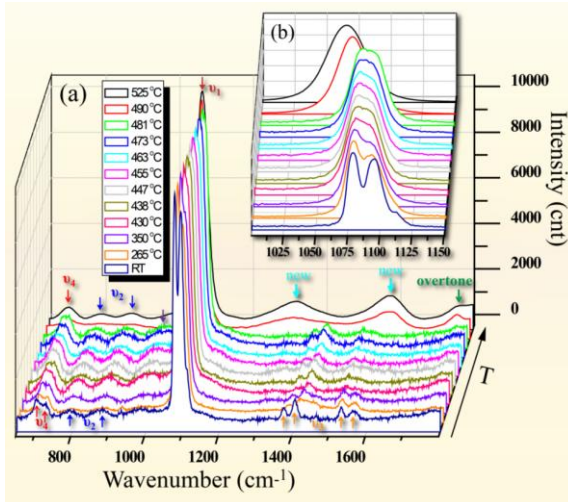


Figure 4 (a) The Raman spectra of (Li/Na)₂CO₃ in the region of 650-1850 cm⁻¹ as a function of temperature in CO₂ atmosphere; **(b)** Magnified view in the region of 1,000-1,150 cm⁻¹

The shift in Raman band with temperature is better viewed in Figure 4 (b), a magnified spectrum showing the region of the major v₁-bands at 1,078 cm⁻¹ and 1,094 cm⁻¹. As the temperature increases, the v₁-bands for Li₂CO₃ and Na₂CO₃ shift toward lower wavenumber and eventually merge into one broad peak at the melting temperature of 490°C. This shift is a direct result of lowered force-constant, elongated C-O bond length and weakened Li(Na)-C-O bond strength by increasing temperature. When the temperature reaches the melting point, the overtone of the out-of-plane bending mode (2*v₂) appears at 1,762 cm⁻¹. It should be noted that a broad but small peak near 970 cm⁻¹ only observed in solid-state carbonates appears not directly related to CO₃²⁻, identification of which is not possible for this study. We speculate that the impurities in the sample could be a source for this unknown peak. A detailed assignment of the measured Raman bands at different temperatures and atmospheres is summarized in Table 1.

The most distinguishable features of Raman spectra in Figure 4 are observed when the carbonate is in a molten state. The four bands corresponding to the v₃ mode disappear from the spectrum while two new broad bands at 1,317 cm⁻¹ and 1,582 cm⁻¹ emerge within the same band width. A natural question to ask is: are these newly emerged Raman bands associated with the C₂O₅²⁻ species?

Table 1 The Raman frequencies measured and assigned for the eutectic (Li/Na)₂CO₃ at selected temperatures and atmospheres

Atmospheres	CO ₂				Air	N ₂
Temperatures (°C)	RT	350	455	490 (molten)	490 (molten)	490 (molten)
Frequencies (cm ⁻¹) v ₄ (weak)	704	706	706	707	707	707
	728	720	715	-	-	-
v ₂ (weak)	792	790	789	790	790	790
	879	879	881	882	885	885
v ₁ (strong)	1,078	1,077	1,077	1,070	1,072	1,072
	1,094	1,090	1,087	-	-	-

	1,375	1,385	1,386	-	1,391	1,392
v_3 (weak)	1,404	1,415	1,416	-	1,421	1,421
	1,531	1,520	1,520	-	-	-
	1,563	1,555	1,545	-	-	-
New peaks (broad)	-	-	-	1,317	-	-
				1,582		
Overtone(2^*v_2)	-	-	-	1,762	1,762	1,762
Unknown	-	-	972	-	-	-

2.3.4 Atmosphere-dependence of Raman spectrum

To answer this question, we first measured Raman spectra in different atmospheres. According to the enabling electrochemical reaction shown in reaction (3), the formation of $\text{C}_2\text{O}_5^{2-}$ requires a source of CO_2 . Figure 5 compares the Raman spectra measured in N_2 , Air and pure CO_2 atmospheres at 490°C where the carbonate is in a molten state. The bands at $1,072 \text{ cm}^{-1}$, 790 cm^{-1} and 885 cm^{-1} , 707 cm^{-1} , $1,391 \text{ cm}^{-1}$ and $1,421 \text{ cm}^{-1}$, $1,762 \text{ cm}^{-1}$ shown in Figure 5 (a) recorded in N_2 atmosphere correspond to the symmetric stretching (v_1), out-of-plane bending (v_2), in-plane bending (v_4), asymmetric stretching (v_3), and the overtone of the out-of-plane bending mode (2^*v_2) vibrations, respectively. The Raman spectrum in air is almost identical to that collected in N_2 . However, the peaks at $1,317 \text{ cm}^{-1}$ and $1,582 \text{ cm}^{-1}$ shown in Fig.14 (c) are only observable in the CO_2 atmosphere.

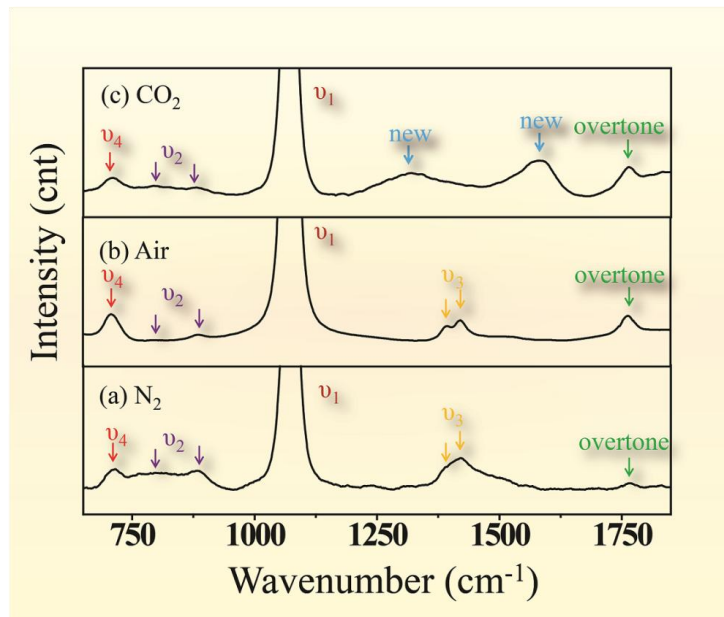


Figure 5: Raman Spectra of CO_2 in Different Atmosphere

The strong CO₂-dependence of the bands at 1,317 cm⁻¹ and 1,582 cm⁻¹ provides a crucial hint for the formation of C₂O₅²⁻ via the CO₂ chemisorption reaction CO₂+CO₃²⁻=C₂O₅²⁻.

2.3.5 DFT Modeling

The theoretical support to the formation of C₂O₅²⁻ is provided by the DFT calculations. The calculations indicate that high Raman activities of C₂O₅²⁻ are within a band width of 1,200-1,600 cm⁻¹. Specifically, the active Raman bands are predicted at 1,366 cm⁻¹, 1,531 cm⁻¹ and 1,566 cm⁻¹ for Li₂C₂O₅ and 1,345 cm⁻¹, 1,547 cm⁻¹ and 1,579 cm⁻¹ for Na₂C₂O₅, respectively. The recorded spectrum in the band width of 1,200-1,650 cm⁻¹ from the MC within 490-525°C in CO₂ atmosphere could, therefore, be an overlap of these characteristic Raman peaks of Li₂C₂O₅ and Na₂C₂O₅ in this band region. To deconvolute the two unique broad peaks around 1,317 cm⁻¹ and 1,582 cm⁻¹, we used Guassian-Lorentizian function with the six theoretical Raman frequencies as the standards. The results are shown in Figure 6, where the black and red lines represent the measured and modeled spectra, respectively. Also shown are the individual spectrum calculated for the pure Li₂C₂O₅ and Na₂C₂O₅, represented by pink and blue lines, respectively. It appears that the modeled spectrum is dominated by the Na₂CO₃; only one peak at 1,566 cm⁻¹ is visible for the Li₂CO₃ while the other two are too weak to be seen. This is primarily due to the differences in size and polarizability of the Na⁺ and Li⁺ ions. Overall, the measured Raman spectrum is in excellent agreement with the DFT calculations if the temperature effect is factored in.

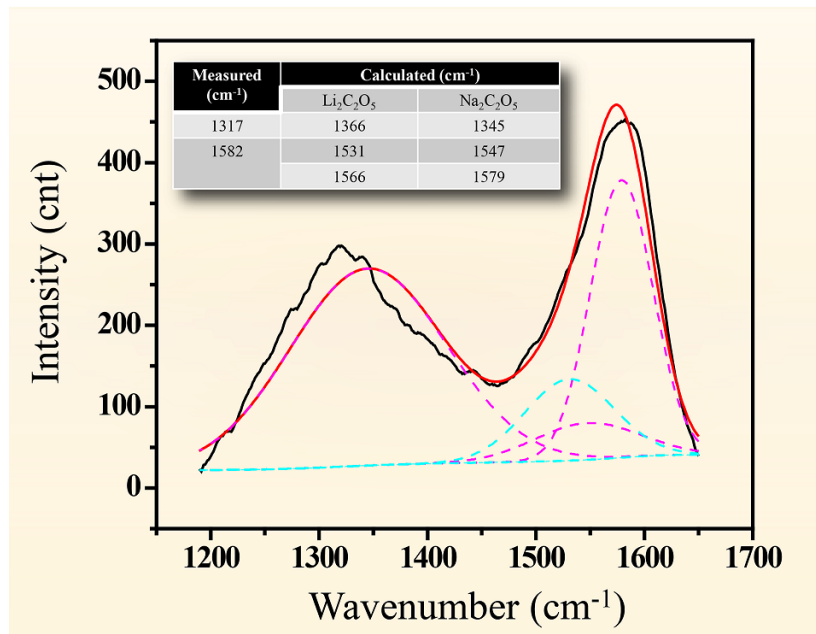


Figure 6: Deconvolution of the two broad bands observed at 1,317 cm⁻¹ and 1,582 cm⁻¹; Inset: the measured and DFT-modeled Raman spectra in a band width of 1,200 - 1,650 cm⁻¹

In summary, we demonstrate the first experimental evidence for the existence of pyrocarbonate C₂O₅²⁻ species in a eutectic Li₂CO₃-Na₂CO₃ melt exposed to CO₂ atmosphere through a combined “DFT modeling” and “Raman Spectroscopy” approach. The existence of C₂O₅²⁻

species is a key support to a new bi-ionic transport model established to elucidate the fundamentals of the high-flux CO₂ transport phenomenon observed in the superior mixed oxide-ion and carbonate-ion conducting CO₂ separation membranes. The broad Raman bands centered at 1,317 cm⁻¹ and 1,582 cm⁻¹ are a characteristic of C₂O₅²⁻ species in molten carbonates exposed CO₂ atmosphere. The measured characteristic Raman frequencies of C₂O₅²⁻ are in an excellent agreement with the DFT-model consisting of six overlapping individual theoretical bands calculated from Li₂C₂O₅ and Na₂C₂O₅.

3. Future Work

The work from the current period has concluded our DFT work on the oxygen reduction in MC and the research will move to next stage using the configuration interaction embedding method. The DFT methods have uncertainties when a charged systems is considered. evidenced by the test case of oxygen on Ag(100). Further studies will be demanded to examine the dependency of DFT hybrid functionals. Even there are many functionals available to choose, but lack of guide for choosing them accordingly to a specific system.

For oxygen diffusion in MC, the DFT study is the first step and provides obtained geometries for the CI studies, which is hard to achieve in CI. We will use the optimized geometry from DFT in the CI calculations.